Journal of Marine Research, 62, 283–312, 2004

Journal of
MARINE RESEARCH

Volume 62, Number 3

Monitoring the meridional overturning circulation in the North Atlantic: A model-based array design study

by Johanna Baehr[1], Joël Hirschi[2], Jens-Olaf Beismann[3,4] and Jochem Marotzke[1]

ABSTRACT

A monitoring system for the meridional overturning circulation (MOC) is deployed into an "eddy-permitting" numerical model (FLAME) at three different latitudes in the North Atlantic Ocean. The MOC is estimated by adding contributions related to Ekman transports to those associated with the zonally integrated vertical velocity shear. Ekman transports are inferred from surface wind stress, whereas the velocity shear is derived from continuous density "observations," principally near the eastern and western boundaries, employing thermal wind balance. The objective is to test the method and array setups for possible real observation in the ocean at the chosen latitudes and to guide similar tests at different latitudes.

Different "mooring placements" are tested, ranging from a minimal setup to the theoretical maximum number of "measurements." A relatively small number of vertical density profiles (about 10, the exact number depending on the latitude) can achieve a reconstruction of the MOC similar to one achieved by any larger number of profiles. However, the main characteristics of the MOC can only be reproduced at latitudes where bottom velocities are small, here at 26N and 36N. For high bottom velocities, in FLAME at 53N, the array fails to reproduce the strength and variability of the MOC because the depth-averaged flow cannot be reconstructed accurately. In FLAME, knowledge of the complete bottom velocity field could substitute for the knowledge of the depth-averaged velocity field.

1. Max Planck Institute for Meteorology, Bundesstrasse 53, 20146 Hamburg, Germany. ***email: johanna.baehr@dkrz.de***

2. School of Ocean and Earth Science, Southampton Oceanography Centre, Southampton SO14 3ZP, United Kingdom.

3. Leibniz-Institut für Meereswissenschaften, IFM-GEOMAR, Düsternbroker Weg 20, 24105 Kiel, Germany.

4. Present address: NEC High Performance Computing Europe GmbH, Prinzenallee 11, 40549 Duesseldorf, Germany.

1. Introduction

The meridional overturning circulation (MOC) carries most of the oceanic heat transport in the Atlantic (Hall and Bryden, 1982). The effect of this northward heat transport of about 1 PW ($= 10^{15}$ W) is seen in the resulting relatively mild climate of western Europe (Ganachaud and Wunsch, 2000). In the Atlantic the MOC is composed of both a (dominating) buoyancy forced contribution, i.e. the thermohaline circulation (THC), and wind-driven meridional transports.

Although the mid-latitude MOC appears to be relatively steady over the last few decades (MacDonald and Wunsch, 1996), palaeoclimatic records suggest that the ocean circulation has undergone rapid changes in the past 120,000 years since the Eemian interglacial period (Heinrich, 1988; Dansgaard *et al.,* 1993; National Research Council (NRC), 2002; Alley *et al.,* 2003). These abrupt changes corresponded to significant variations in temperature and climate over the North Atlantic and its adjacent regions. Changes in the Atlantic MOC are eminently associated with the proposed mechanisms of such abrupt climate change (Marotzke, 2000). A weakening or collapse of the Atlantic MOC might entail a reduction in the North Atlantic heat transport which in turn would correspond to significant variations in temperature and climate over the North Atlantic and its adjacent regions. The suggested mechanisms are of concern for both past and future changes. Predicting whether a conceivable rapid change in the MOC is impending is as important as detecting such an ongoing change.

Currently, ship-based transoceanic sections yield the most reliable estimates of the MOC, but provide only snapshots of the MOC and the related meridional transports, e.g. Hall and Bryden (1982); Ganachaud and Wunsch (2000). Repeated hydrographic sections might allow decadal changes in the MOC to be detected (Deutsch *et al.,* 2002), but they are too expensive and personnel-intensive to ensure a continuous observation of the MOC.

An alternative monitoring strategy, which is more cost-effective than ship-borne measurements, was suggested by Marotzke *et al.* (1999). Their conceptual starting point is the thermal wind relationship, which links density differences to the zonally averaged meridional flow. Marotzke (1997) and Marotzke and Klinger (2000) based a theory of a purely buoyancy-driven MOC on the ability to express the meridional streamfunction as a function of latitude and density difference between eastern and western sidewalls (and other independent parameters). In principle, only the systematic observation of density at eastern and western sidewalls would be required to monitor the MOC continuously (Marotzke *et al.,* 1999).

Thus, Marotzke *et al.* (2002) suggested the implementation of a mooring array for continuous density observation to monitor the MOC at 26N. The design of the observing array was tested in two eddy-permitting numerical ocean models (Hirschi *et al.,* 2003), estimating the MOC from zonal density differences and wind information only. However, 26N is unique in its geographical setup: the circulation is separated into a geographically detached western boundary current (in the Florida Strait), a confined western boundary current (the Antilles Current) and a basin-wide return flow. This study, therefore, aims to

establish how generally valid the configuration at 26N is and if this approach could be applied to other less special latitudes in the North Atlantic.

In the present study (as in Hirschi *et al.,* 2003), the monitoring array is "deployed" into a numerical model assuming that the implementation of the real field experiment could be improved considerably by "monitoring" the MOC in a model. Efficient experiment design (or more specifically array design) has been argued to play a key role in obtaining the maximum information from available resources (McIntosh, 1987; Barth and Wunsch, 1990) since oceanographic measurements are costly and difficult to obtain. Simulating the performance of observing arrays in numerical models has been conducted based on two different intentions. A variety of design studies were performed to optimize a monitoring strategy, whereas other work addressed the fundamental principles of observing system design. Both types of array design studies can be classified based on the chosen criterion to measure the capability of the particular array (Hackert *et al.,* 1998):

(i) The most intuitive approach might be to employ statistical techniques, e.g. error estimates, as a measure of the capability of the array: Bretherton *et al.* (1976) used the objective mapping approach—widely used in meteorology—to design a current meter array for the MODE program (Mid-Ocean Dynamics Experiment). Barth and Wunsch (1990) analyzed the design of acoustic tomographic arrays using simulated annealing for an idealized (two-dimensional) case. Drifter launch strategies, i.e. involving advection of the observing sites, based on Lagrangian templates were investigated by Poje *et al.* (2002) who aimed to establish a criterion requiring a minimal amount of *a priori* information. Guinehut *et al.* (2002) applied the objective mapping approach to design an array of profiling floats in the North Atlantic, comparing Eulerian and Lagrangian arrays.

(ii) Alternatively, data assimilation techniques were used to quantify the information content of an array (McIntosh, 1987). Bennett (1985) used the variational inverse method of Bennett and McIntosh (1982) to assess the efficiency of arrays composed of pressure transducers and acoustic tomography units. Hackert *et al.* (1998) used a data assimilation scheme to optimize the location of a limited number of moorings for the proposed Pilot Research Moored Array in the Tropical Atlantic (PIRATA).

(iii) Sensitivity studies of a model can be used to derive a statement about the best observational strategy: Schröter and Wunsch (1986) calculated the sensitivity of their objective function to changes in the data; mapping the values of the used set of Lagrange multipliers allowed them to determine the regions of greatest sensitivity of the objective function to particular measurement types. Harrison *et al.* (1989) conducted a similar sensitivity study for the tropical Pacific Ocean. Although not specifically aligned to observing system design, this study was—together with Harrison (1989)—crucial in identifying the latitudinal extent of the Tropical-Atmosphere-Ocean (TAO) array wind measurements. Recently, adjoint sensitivity

studies have been used to identify regions where (additional) observations should take place, explicitly not confined to near-surface observations and hydrographic sections only. Marotzke *et al.* (1999) studied adjoint sensitivities of the oceanic heat transport to dynamically link hydrographic measurements and heat transport estimates. Köhl and Stammer (2004) conducted an adjoint sensitivity study to determine an optimal observing array to monitor transport changes across the Greenland-Scotland ridge.

All the studies mentioned above regard array design as an optimization problem either by optimizing the array itself or by taking a general view toward the underlying principles of array design. Generally, model-based pre-deployment array design does not seem to have been used widely. A notable exception is Hackert *et al.* (1998), who conducted a series of observing system simulations, testing the ability of the respective sample array to resemble actual TOPEX/Poseidon data. In contrast, the present study seeks to test a monitoring strategy, primarily aiming to provide immediate support for a realizable observational campaign. Hirschi *et al.* (2003) provided support for a MOC monitoring strategy at 26N. Here, we investigate whether other less geographically special latitudes are suitable for a similar strategy. For this, we analyze in detail the force balance of the MOC, and how it varies with latitude and geometry.

This paper is organized as follows. Section 2 provides a description of the employed method and the numerical model used. The array design for the different latitudes, the results from different array setups and an analysis of the weaknesses of the monitoring arrays are found in Section 3. The ability of the array to estimate the heat transport variability is tested in Section 4. Section 5 contains a discussion and conclusions follow in Section 6.

2. Method and model

a. Method

The approach applied here is the same as used by Hirschi *et al.* (2003) and Hirschi and Marotzke (2004), who employed Lee and Marotzke's (1998) decomposition of the meridional velocity field. The MOC is described as the sum of contributions originating from two measurable quantities: the zonal density difference and the surface wind stress. Thermal wind balance is assumed to hold everywhere. For a rectangular basin, i.e. zonally uniform topography and vertical sidewalls, the zonal integration of thermal wind leads to

$$L_x \overline{\frac{\partial v(x, y, z)}{\partial z}} = -\frac{g}{\rho_0 f}(\rho(x_W, y, z) - \rho(x_E, y, z)), \tag{1}$$

where L_x is the zonal extent of the rectangular basin, $\rho(x_W, y, z)$ and $\rho(x_E, y, z)$ are the densities at the eastern and western sidewalls, respectively, and the overbar indicates the zonal average (Marotzke *et al.,* 1999). Further, v is the meridional velocity, g the acceleration due to gravity, f the Coriolis parameter and ρ_0 a reference density. Under

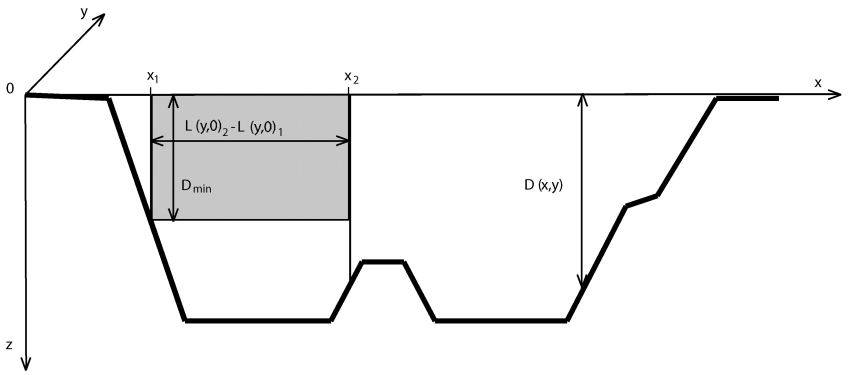

Figure 1. Schematic of a zonal transect with two profiles ($n = 1$ and $n = 2$) at the locations x_1 and x_2, respectively. The distance between the two profiles is $L(y, 0)_2 - L(y, 0)_1$. $D(x, y)$ denotes a depth profile along the section. The shaded square indicates where thermal wind (according to Eq. 2) is described by the two profiles. The velocities outside this area are initially set to zero.

realistic circumstances, in particular in the presence of irregular topography, we expect that a number of density profiles is required, denoted $n = 1, 2, \ldots, N$. Vertical integration of Eq. (1) yields an expression for the meridional velocity field between the two vertical profiles n and $n + 1$ at a zonal distance $L(y, 0)_{n+1} - L(y, 0)_n$. A depth-dependent meridional velocity field $v_{g_n}(x, y, z)$ is defined as

$$v_{g_n}(x, y, z) = \begin{cases} -\dfrac{g}{\rho_0 f}\left[\displaystyle\int_{-D_{min}}^{z}\left(\frac{\rho(x_{n+1}, y, z) - \rho(x_n, y, z)}{L(y, 0)_{n+1} - L(y, 0)_n}\right)dz\right] & \text{for } -D_{min} \le z < 0 \\ & \text{and } x_n \le x \le x_{n+1}, \\ 0 & \text{for } -D(x, y) \le z < -D_{min} \\ & \text{and } x_n \le x \le x_{n+1}, \\ 0 & \text{for } x < x_n \text{ or } x > x_{n+1}. \end{cases} \tag{2}$$

Here, $D(x, y)$ denotes a depth profile along the zonal section, and D_{min} is the minimum depth found between the two profiles (in the interval $x_n \le x \le x_{n+1}$). Figure 1 depicts the example for $N = 2$, the shaded square indicates, where thermal wind (Eq. 2) is described by the two profiles. Generally, Eq. (2) describes thermal wind in the area between the profiles n and $n + 1$, with zero velocity everywhere else within the zonal transect. In the presence of zonally nonuniform topography, bottom triangles occur when the maximum depth of the area between the two profiles is larger than the maximum depth common to both profiles, or the minimum depth of the area between the two profiles is smaller than the maximum depth common to both profiles. Initially, the velocity is set to zero at depths greater than D_{min} and at longitudes smaller than $L(y, 0)_n$ or larger than $L(y, 0)_{n+1}$. A level of no motion is assumed to be at the bottom of the ocean. For an ocean basin covered

by N vertical density profiles, the complete meridional velocity field is then the sum of the velocity fields between two adjacent profiles:

$$v_g(x, y, z) = \sum_{n=1}^{N-1} v_{g_n}(x, y, z). \tag{3}$$

Further zonal and vertical integration gives the density-driven contribution of the overturning streamfunction (Marotzke, 1997), which exists if no mass enters or leaves through the boundaries. To ensure zero net meridional mass transport, without distorting the local velocity shear, a spatially (but not temporally) constant correction is applied first (Hall and Bryden, 1982), yielding a corrected meridional velocity field $v_{g_{corr}}(x, y, z)$:

$$v_{g_{corr}}(x, y, z) = v_g(x, y, z) - \frac{\int_{-D(x,y)}^{0} \int_{0}^{L(y,z)} v_g(x, y, z)dxdz}{A}, \tag{4}$$

where A is the area of the cross-section. The resulting corrected meridional velocity field maintains mass balance and can thus be integrated vertically and zonally to yield the density-driven meridional overturning streamfunction as a function of latitude and depth.

The wind-driven part of the MOC can be calculated based on the Ekman volume transport,

$$v_{ek}(x, y, z) = -\frac{1}{\rho_0 f A_d} \int_0^{L(y,0)} \tau(x, y)dx, \tag{5}$$

where $\tau(x, y)$ is the x-component of the wind stress, assuming an Ekman depth d (covering the zonal area A_d) to which the Ekman transport is confined. Typically, d is 50–100 m, e.g. Chereskin *et al.* (1997). To ensure no net meridional mass transport related to the zonal wind stress, the flow through the Ekman layer is compensated by a depth-uniform return flow (Jayne and Marotzke, 2001). The corrected velocity field reads as follows:

$$v_{ek_{corr}(x,y,z)} = \begin{cases} v_{ek} - \dfrac{v_{ek}A_d}{A} & \text{for } -d \geq z \\ -\dfrac{v_{ek}A_d}{A} & \text{for } -d < z \end{cases}, \tag{6}$$

where A is the area of the zonal transect. Integrating the corrected Ekman velocities yields an overturning contribution, which is zero at the surface and at the bottom of the ocean, and has its maximum transport at the Ekman depth. Note that the zonal wind stress also generates a depth-dependent geostrophic flow as it affects the density gradients (McCreary and Lu, 1994), which is included in the reconstruction based on the density profiles.

The reconstructed overturning is the sum of the density- and wind-driven components

based on the corrected velocities $v_{g_{corr}}(x, y, z)$ and $v_{ek_{corr}}(x, y, z)$ given in Eqs. (4) and (6), respectively:

$$\Psi(y, z) = \int_{-D(x,y)}^{z} \int_{0}^{L(y,z)} v_{g_{corr}}(x, y, z)dxdz + \int_{-D(x,y)}^{z} \int_{0}^{L(y,z)} v_{ek_{corr}}(x, y, z)dxdz. \quad (7)$$

This MOC reconstruction could be based on real measurements, where $v_g(x, y, z)$ could be obtained from vertical density measurements (e.g. an array of full depth moorings measuring temperature and salinity) and $v_{ek}(x, y, z)$ could be obtained from satellites measuring near-surface wind speed and direction. Both $v_g(x, y, z)$ and $v_{ek}(x, y, z)$ need to be corrected to maintain mass balance (as described in Eqs. (4) and (6)). Note that this MOC reconstruction is identical to a reconstruction in which the wind and the density velocity fields would be added prior to the correction ensuring mass balance. Correcting the two contributions separately greatly aids in their interpretation.

b. The FLAME model

The model output used in this study stems from the 1/3° Atlantic Model of the FLAME group, a hierarchy of Atlantic Ocean models (Dengg *et al.,* 1999; Beismann and Redler, 2003). The code is based on a refined configuration of the Geophysical Fluid Dynamics Laboratory's (GFDL) MOM, version 2.1 (Pacanowski, 1995). The model is so-called "eddy-permitting," meaning that the horizontal grid resolution is high enough to allow the formation of oceanic eddies, without, however, properly resolving the deformation radius at all latitudes. The model domain extends from 70S to 70N, and from 100W to 30E. It has open boundaries across the Antarctic Circumpolar Current in the Drake Passage and south of Africa at 30E. The northern boundary is closed with a restoring zone at 70N. FLAME has a realistic bottom topography, and a rigid lid condition is applied at the surface. The horizontal resolution is 1/3° in longitude and 1/3° × cos (ϕ) in latitude (ϕ), similar to the DYNAMO intercomparison study (Willebrand *et al.,* 2001). FLAME's deep water formation and meridional overturning are enhanced due to the implementation of a higher vertical resolution (45 non-equidistant levels), together with the adaptation of a bottom boundary layer scheme (Beckmann and Döscher, 1997) and lateral subgrid scale mixing along isopycnals (Redi, 1982; Cox, 1987).

The model integration starts at 01 January 1900. The atmospheric forcing is based on the ECMWF (European Centre for Medium Range Weather Forecast) re-analysis (Barnier *et al.,* 1995) monthly means, but has superimposed wind and heat flux anomalies from NCEP-NCAR (National Centers for Environmental Prediction/National Center for Atmospheric Research) re-analyses products (Kalnay *et al.,* 1996) for the period from 1958 to 2001. This superposition of forcing components has been described in detail in Eden and Willebrand (2001). For the freshwater fluxes, sea-surface salinity is restored to a combination of the climatological values of Levitus *et al.* (1994) and Boyer and Levitus (1997) (see

Beismann and Redler (2003) for details). For the analysis conducted here, the model output used starts at 01 January 1980 and has a total length of 20 years.

c. Data set

A subset of three different latitudes is chosen from FLAME: 26N, 36N, and 53N. The starting point is 26N as used by Hirschi *et al.* (2003). The two additional latitudes are chosen to test if the employed method is reliable at places with a less special geographical and dynamical setup than 26N. Hence, 36N represents a subtropical latitude as does 26N, with the significant difference that the western boundary current is no longer geographically confined to a shallow strait. As 36N was subject to observations, e.g. Roemmich and Wunsch (1985), a comparison of model and data is possible. The latitude of 53N, in contrast, is situated at the boundary to the subpolar gyre and exhibits much weaker stratification than the two subtropical latitudes. It was observed by different hydrographic sections Dobrolyubov *et al.* (2002); Talley (2003), but more important its western boundary was recently subject to intense observations (Fischer *et al.,* 2004). This allows—together with an analysis of the dynamics of the subpolar gyre in FLAME (Scheinert, 2003)—a comparison of the model and the observed meridional velocity field. The geographical setup of the three latitudes (and the whole North Atlantic) is similar in that the Mid Atlantic Ridge (MAR) divides the basin. However, there are pronounced differences regarding the steepness of the slopes at the margins and the absolute depth of the basin at the specific latitude.

Figure 2 shows the topography and the time-mean meridional velocity field for the three different latitudes. All three sections exhibit a strong surface western boundary current, albeit differing in their vertical structures and their narrowness and mean flow direction. Note that at 36N FLAME does exhibit a strong northward western boundary current, but the deep southward flow is not found at the western boundary (here, strong southward velocities are found at the surface). Instead, the highest deep southward meridional velocities occur along the western slope of the MAR (cf. Fig. 2). The section by Roemmich and Wunsch (1985), in contrast, suggests a western boundary current situated beneath the northward surface current with maximum velocities of 0.5 cm s^{-1}.

For all three investigated latitudes the basin is, apart from the boundaries, dominated by the return flow which differs considerably between the latitudes in its (local) strength. The maximum overturning is 16 Sv at 26N, 17 Sv at 36N, and 14 Sv at 53N. In FLAME the maximum overturning of about 18 Sv is found at 40N at a depth of about 1000 m, which is largely in accordance with observations (MacDonald, 1998; Ganachaud and Wunsch, 2002). The mean Ekman transport is positive, i.e. northward, for 26N (2 Sv), but negative for 36N (−2 Sv) and 53N (−3 Sv).

Time mean values of the meridional heat transport in FLAME are slightly lower than observations at the two subtropical latitudes. The 26N value of 0.9 PW is notably smaller than the 1.2 PW estimate of Hall and Bryden (1982), Roemmich and Wunsch (1985) and Lavin *et al.* (1998) and the 1.3 PW estimate by Ganachaud and Wunsch (2000) and Talley

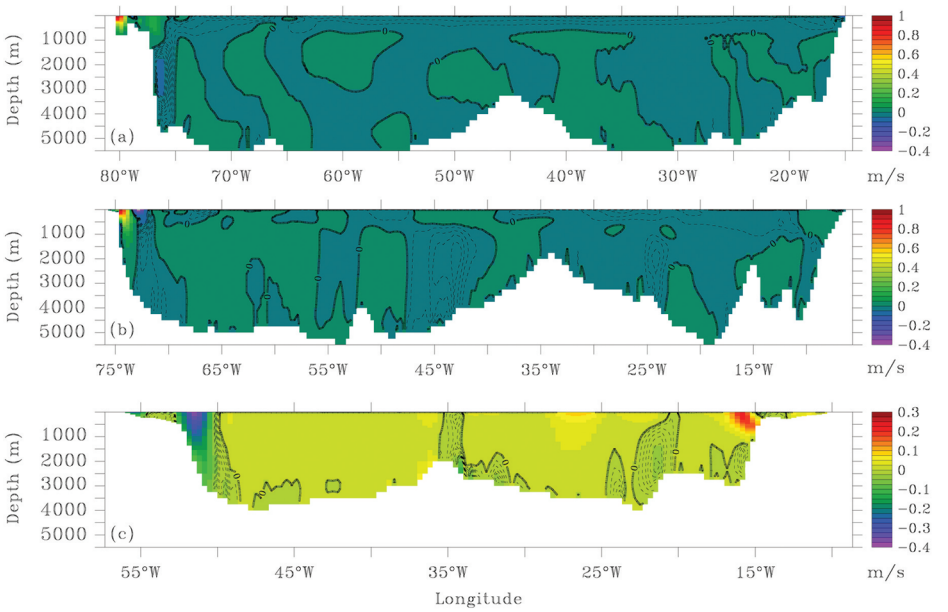

Figure 2. Time-mean meridional velocity field from FLAME for (a) 26N, (b) 36N and (c) 53N (20-yr average). Note that the color scale is linear, but the contour lines are only plotted for velocities between -0.05 and 0.00 m s^{-1} (in intervals of 0.01 m s^{-1}) for all latitudes to enhance the visibility of the southward meridional velocities.

(2003). The 36N value of 0.8 PW is similar to the estimate by Roemmich and Wunsch (1985) and Talley (2003), but considerably smaller than the estimate of 1.2 PW by Sato and Rossby (2000). The 53N value of 0.65 PW agrees with the 0.62 PW estimate of Talley (2003), which is based on a 1962 hydrographic section. The seasonal variability of the meridional heat transport is, however, in close agreement to the expectations (Böning *et al.,* 2001). Generally, FLAME's meridional transports and their variability in the North Atlantic are—with all its inevitable limitations—comparable to observations (Willebrand *et al.,* 2001; Böning *et al.,* 2001).

3. Results

The MOC is reconstructed based on density differences and the surface wind stress, as described in Section 2a. The starting point is the array setup for 26N as it was used by Hirschi *et al.* (2003). For the two additional latitudes, comparable array setups are investigated, adapting a (financially) feasible number of "moorings" only. As in Hirschi *et al.* (2003) the criteria for the placement of these density profiles are a combination of experience and qualitative application of some sampling theorems: the profiles need to be placed particularly in areas of high meridional velocities, but the resulting array needs to cover as much of the basin area as possible in order to minimize remaining bottom

triangles. The latter criterion is based on the assumption that the vertical structure of the MOC can only be reconstructed when the basinwide (weak) return flow is captured, too. Hence, this "mooring" placement does rely on prior knowledge about the "distribution" of the quantity (in this case the meridional velocity field) taken from the numerical model.

Thus, the placement of the profiles is initially based on physical intuition only. Similarly, most other studies rely on the trial-and-error adjustment of array configurations (Bretherton *et al.,* 1976), sometimes stating that it is "clearly impossible to test every possible array" (McIntosh, 1987); two notable exceptions are Barth and Wunsch (1990) and Barth (1992) who analyzed idealized cases. Here, no systematic attempt is made to optimize the "mooring" placement. Rather, we want to demonstrate that our chosen design captures the quantity of interest, the MOC. However, the intuition-based array is later justified with a technical array design study.

a. The standard observing array

A basic array is now designed; as argued before, we cannot currently optimize it rigorously. Instead, we follow the two physical criteria described above and the practical requirement of financial feasibility if the design is implemented. The westernmost part of the basin exhibits a strong western boundary current, hence the western margin of the basin needs dense coverage, which was initially set to four profiles: the first one covering the shallow part of the current, the second one located in the center of the boundary current, the third one placed at the edge of the time-mean current and the fourth one just outside the western boundary current. Apart from the western margin the rest of the basin is dominated by the return flow; the eastern part of the basin is, hence, initially covered with three profiles, placed along the slope. To account for pressure differences on both sides of the MAR, two more profiles are placed on the eastern and western slope of the ridge. The basic array consists of nine profiles, placed across the transect with higher coverage at the margins.

Taking into account the specific dynamical and geographical setup of each latitude this basic array is modified for each of the considered latitudes (26N, 36N and 53N in the North Atlantic), to set up a standard array for each individual latitude. Figure 3 shows the placement of the profiles on each transect. The basic array as well as its local modifications are summarized in Table 1.

At 26N the western boundary current is geographically confined to the Florida Strait. In the real world this latitude is comparatively well-investigated as it is close to the latitude of four modern hydrographic sections (1957, 1981, 1992, 1998; cf. McTaggert *et al.* (1999) and e.g. Koltermann *et al.* (1999)). Furthermore, it offers a unique long-term time series of western boundary current observations as the mass transport across the Florida Strait has been monitored by cable measurements for over 20 years (Larsen, 1985; Baringer and Larsen, 2001). To account for this, the basic array is extended by assuming the total mass transport at the longitudes of the Florida Strait to be known at all times. The velocity pattern is updated every three months; inaccuracies in the cable measurements are

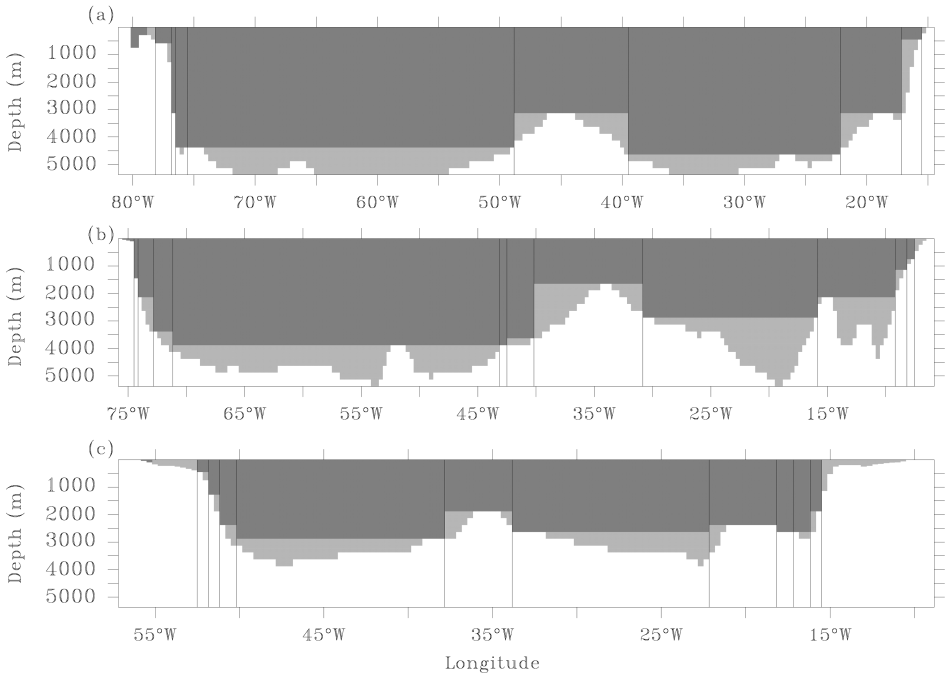

Figure 3. Placement of profiles for the standard array: (a) 26N, (b) 36N and (c) 53N.

mimicked by added noise of 1 Sv standard deviation. This setup is identical to the one used in Hirschi *et al.* (2003).

Farther north, the western boundary current is no longer geographically confined. At 36N a strong surface northward boundary current can be found at the western boundary in FLAME, but the deep southward flow (as pointed out in Section 2c) is found at the slope of the MAR. Whereas observations show a deep southward flow at the western boundary underneath the northward surface current (Roemmich and Wunsch, 1985), a similar velocity distribution as in FLAME has resulted from a CO_2 increase in a coupled GCM (Wood *et al.,* 1999). Therefore, such a distribution needs to be covered by the method (assuming prior knowledge of the velocity information for the placement of the profiles). Hence, the basic array for 36N is extended by two profiles covering the deep southward flow along the western slope of the MAR. Secondly, the array is enhanced by one

Table 1. Basic array and its modifications for the individual latitudes.

Latitude	W Boundary	MAR	E Boundary	Total No. of Profiles
26N	4 + Florida Strait	2	3	9 + Florida Strait
36N	4	2 + 2	3 + 1	12
53N	4	2	3 + 2	11

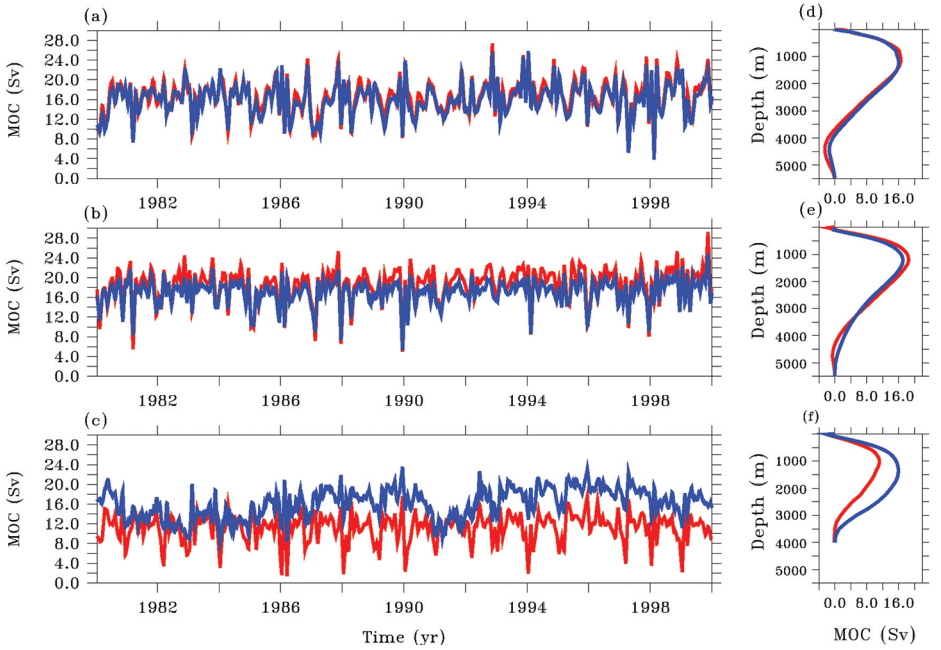

Figure 4. MOC (red) and estimated transport (blue) on the basis of the standard arrays. The estimated transport is the sum of the thermal wind and Ekman contributions. Timeseries of the maximum transports are shown in panels (a)–(c), and a time-mean vertical profile in panels (d)–(f); 26N: (a) and (d), 36N (b) and (e), 53N: (c) and (f).

additional profile at the eastern margin to ensure coverage of the high velocities over the relatively gentle slope. Thus, the standard array for 36N consists of 12 profiles, three profiles more than the basic array at 26N.

The third and northernmost latitude, 53N, does not show a northward western boundary current, but currents are stronger at the eastern and western boundary than in the rest of the basin. Furthermore, the eastern slope is relatively gentle, so the basic setup of three profiles is not sufficient to cover the strong currents here. The basic array is supplemented with two extra profiles.

b. MOC reconstruction based on the standard array

The MOC is reconstructed based on the "standard arrays" for the different latitudes, where the density is "measured" at the locations of the profiles; knowledge about the surface wind stress is assumed for the zonal transect. Figure 4 shows the MOC calculated from the model velocities and the MOC reconstruction based on the standard arrays. It shows that for 26N and 36N, the mean value of the maximum overturning and its strong temporal variability are largely captured. For 36N the mean value is underestimated by about 1 Sv; the variability of the reconstruction is slightly too weak (by about 3 Sv for the

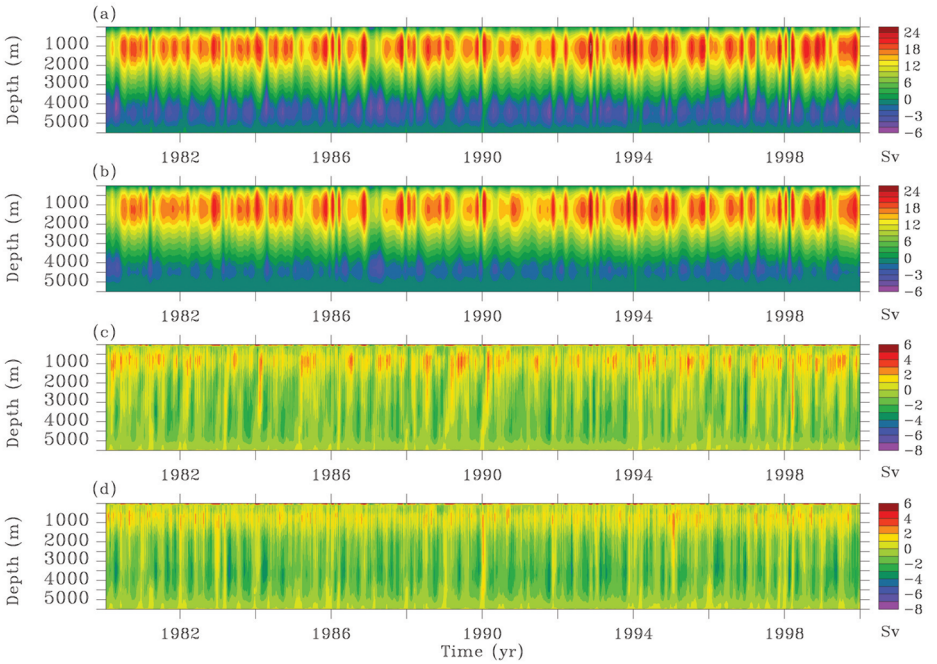

Figure 5. Time series for 26N: (a) MOC, (b) reconstruction based on the standard array, (c) MOC minus reconstruction based on the standard array, (d) MOC minus reconstruction based on a profile at every zonal grid cell. Note that the color scale in panels (a) and (b) is finer for negative transports.

maximum amplitudes). The time-mean vertical profile reveals that for both latitudes the deep return flow is underestimated. For 53N the quality of the reconstruction of the maximum varies with time: whereas in some years the mean value of the maximum is met precisely, the overturning is overestimated at most times. The time-mean vertical structure indicates that the maximum MOC is not reproduced in its magnitude nor in its position within the water column.

A more detailed picture is provided using Hovmoeller diagrams as they show the evolution of the full-depth overturning over time, rather than the time-mean vertical profiles (as in Fig. 4). Figures 5 (26N), 6 (36N) and 7 (53N) show the model overturning (panel a) and its reconstruction based on the respective standard array (panel b). For the two subtropical latitudes the overturning is captured both in its temporally varying magnitude and its vertical extent. Temporal mis-estimates occur in the upper 3000 m (cf., panel c, Figs. 5 and 6), but the reconstruction of the deep southward flow is generally too weak by about 1.5 Sverdrups. At 53N, in contrast, the overturning is overestimated. The structure of the deep southward flow is not captured, which might be predominantly due to the overestimate of the maximum, since the model shows no distinctive deep southward current at 53N. Overall, the MOC reconstruction based on the standard array follows the

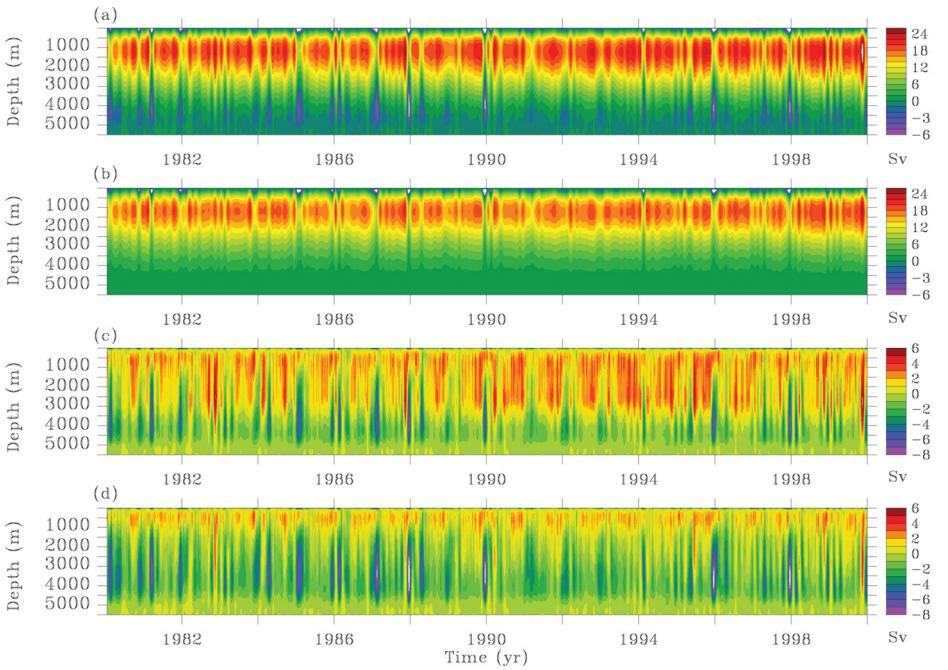

Figure 6. Time series for 36N: (a) MOC, (b) reconstruction based on the standard array, (c) MOC minus reconstruction based on the standard array, (d) MOC minus reconstruction based on a profile at every zonal grid cell. Note that the color scale in panel (a) and (b) is finer for negative transports.

original MOC closely for 26N and 36N, whereas larger—temporally variable—differences occur at 53N (about 1/3 of the total strength of the MOC there). Note that the reconstruction appears to be robust to small zonal variations in the placement of the standard array profiles, e.g. one or two grid cells.

The errors in the reconstruction could originate from the sparse resolution of the profiles or from conceptual limits of the method, or both. To analyze this, the MOC is reconstructed based on the maximum amount of available information. In Figures 5, 6 and 7 (panel d) the Hovmoeller diagrams for the differences between original and reconstruction are shown, relying on the (theoretical) maximum amount of measurements, i.e. a full-depth "mooring" at every zonal nonland grid point. Comparing the reconstruction of the standard array and the one relying on maximum amount of density information shows that the quality of the reconstruction in the upper part of the water column improves for all latitudes, most notably for 53N where the bias in the reconstruction is now nearly temporally constant (about 4 Sv). In all cases, the underestimate of the deep return flow is not due to the sparse basin-coverage of the array. Hence, both sources of errors are investigated: first, variations in the number of profiles and second, the dynamical limits of the method are analyzed.

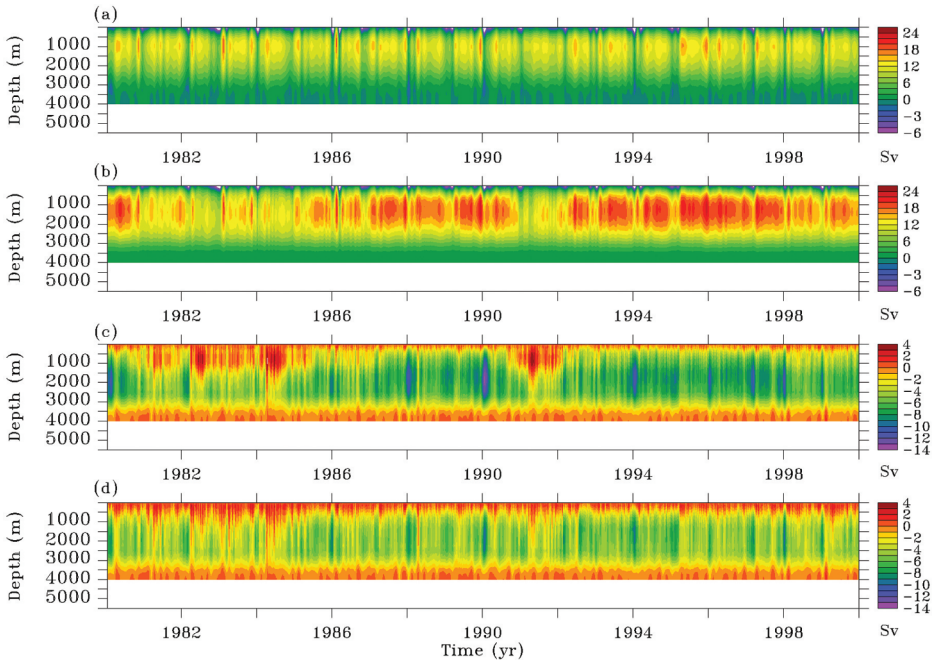

Figure 7. Time series for 53N: (a) MOC, (b) reconstruction based on the standard array, (c) MOC minus reconstruction based on the standard array, (d) MOC minus reconstruction based on a profile at every zonal grid cell. Note that the color scale in panels (a) and (b) is finer for negative transports.

c. Variations in the number of profiles

The robustness of the placement of the profiles employed in the standard array is tested, analyzing the results using fewer and larger numbers of profiles. Figure 8 summarizes the different setups and their respective results. The robustness of the placement of the profiles employed in the standard array is tested, analyzing the results using fewer and larger numbers of profiles. Figure 8 summarizes the different setups and their respective results. The number on top of the profile indicates its rank order in the setup, starting from a simple setup of two profiles, one each at the eastern and western boundaries. Then, profile number 3 is added, then 4 and so on. The very last point represents the result using all available model density information. The quality of the reconstruction is quantified in terms of the correlation coefficient, the rms error of the timeseries of the maximum and the rms error of the time-mean vertical profile.

For 26N the correlation coefficient shows little dependence on the number of profiles used. The reconstructed density-driven contribution does not vary with periods longer than about a year, but its absolute value is sensitive to the number of profiles used. Thus, the correlation coefficient is dominated by the short-term variability of the reconstruction, i.e., the estimated wind-driven contribution, which itself is independent of the number of

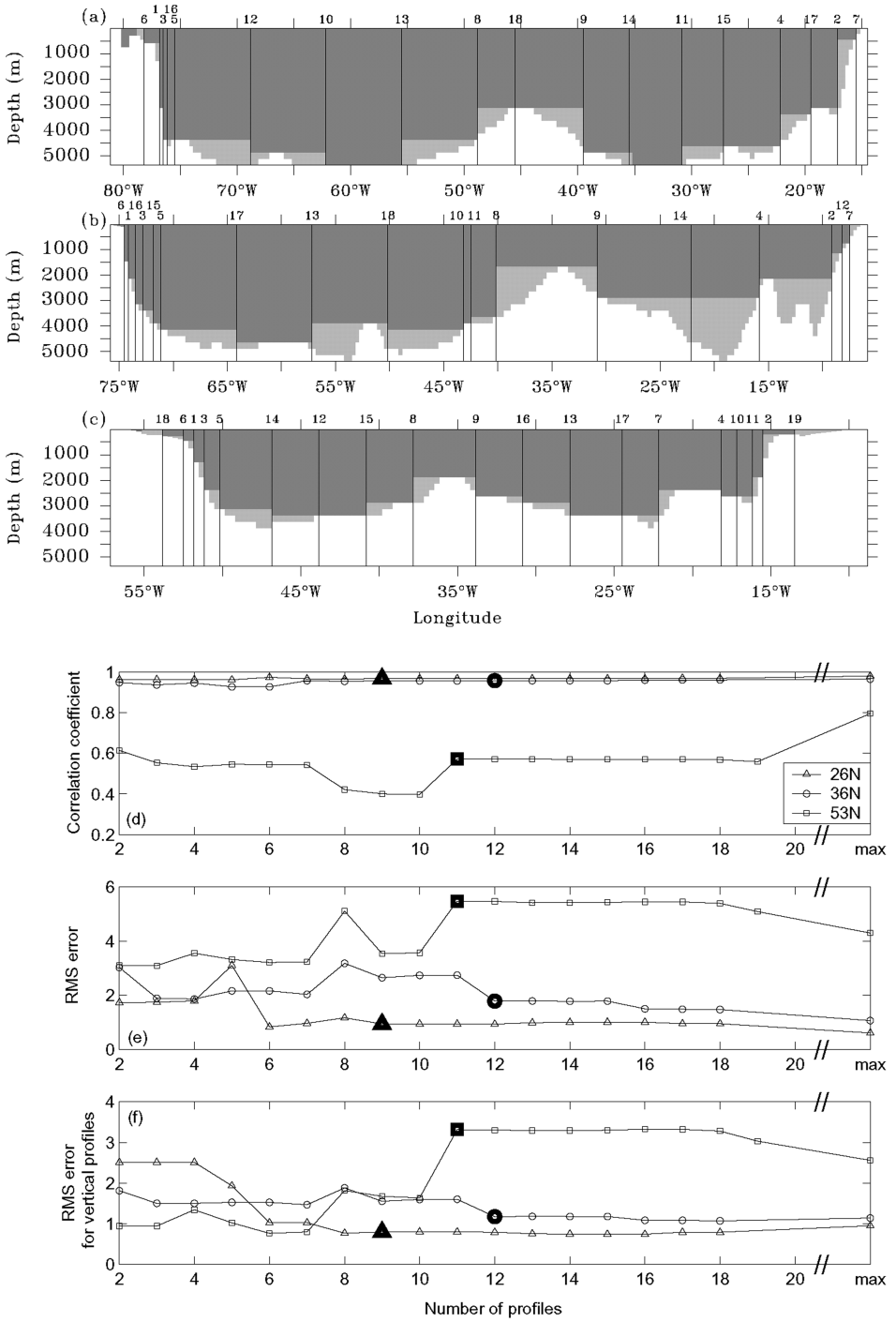
(a)
(b)
(c)
Depth (m)
1000
2000
3000
4000
5000
80°W
70°W
60°W
50°W
40°W
30°W
20°W
75°W
65°W
55°W
45°W
35°W
25°W
15°W
Longitude
Correlation coefficient
RMS error
RMS error
for vertical profiles
(d)
(e)
(f)
26N
36N
53N
max
Number of profiles

density profiles used. The rms error is small as well, with the exception at five profiles, where the three profiles at the western margin cover the strength of the deep southward flow, but not yet (as with six profiles) the northward flow in its total strength. This is mirrored in the rms error of the vertical profile, which decreases strongly until six profiles are used and is saturated when nine profiles are placed.

36N exhibits generally similar characteristics: The correlation coefficient does not vary significantly between the different setups, whereas the rms error for both the timeseries of the maximum and the time-mean vertical profile shows sensitivity to the different setups. Most distinctive is the decrease in the quality of the reconstruction (measured by the rms error) between 8 and 11 profiles, which is due to the combination of the underestimate of both the deep southward flow (on the western slope of the MAR) and the eastern boundary current. The rms errors are not constant until the array covers both the MAR and the shallow eastern slope (with a total of 12 profiles then).

In contrast to the two other latitudes, the correlation coefficient at 53N is sensitive to the number of profiles used. The low-frequency part (with periods longer than about a year) of the thermal wind contribution varies with time, and the estimated variability of the thermal wind contribution varies with the number of profiles used. Note that the overturning itself has a temporally constant low-frequency contribution. For a rudimentary array of seven profiles or fewer, the correlation coefficient of about 0.55 is due to a temporally nonvarying estimate of the thermal wind contribution (and a correct estimate of the wind contribution).

With 7 to 10 profiles, the low-frequency part of the thermal wind is at certain times estimated correctly; whereas at others, the reconstructions fail by as much as 10 Sv. Hence, the correlation coefficient is smaller than with a fewer number of profiles and the rms error is larger (for both the time series of the maximum and the vertical profile). Note that the reconstruction using all model information has a higher correlation coefficient than achieved with any number of profiles, and a (slightly) smaller rms error for the time series of the maximum and the time-mean of vertical profile than achieved with 11 profiles.

It is only seemingly paradoxical that at 53N the reconstruction becomes worse when a higher number of profiles is used. One needs to distinguish between the quality of the

←

Figure 8. Top: Placement of profiles, (a) 26N, (b) 36N and (c) 53N. The number on top of the profile indicates its rank order in the setup. The standard setup (indicated by a bold marker) is derived from a simple setup of two profiles, adding first another profile each at the western and eastern boundary. Second, coverage at the western margin is intensified by two profiles; third, the two MAR profiles are included, and a (shallow) eastern profile plus the individual modifications for the latitudes complete the standard array setup. Additional profiles are placed in the middle of the remaining gaps (up to 18 profiles in total). Bottom: (d) correlation coefficient, (e) rms error for the time series of the maximum MOC, and (f) rms error for time-mean vertical profile based on different setups. The very last point represents the maximum amount of profiles, i.e. using all available model density information, which is 196 profiles for 26N, 208 profiles for 36N and 139 profiles for 53N, respectively.

reconstruction of the total MOC and the quality of the reconstruction of the thermal wind contribution. With more profiles, the thermal wind reconstruction gets closer to the thermal wind reconstruction that is based on the maximum number of profiles. However, this does not necessarily mean that the reconstruction of the total MOC improves. In particular, errors in the reconstruction arise if the assumption of small bottom velocities is invalid. One indication of this is that the low-frequency part of the thermal wind contribution at 53N varies with time, but the low-frequency part of the MOC does not. Thus, a setup with seven profiles or less does not capture the basic characteristics of the MOC for the right reasons, it merely benefits from the coincidental compensation of neglected factors.

In summary, at 26N and 36N the standard array is the minimal setup allowing a reliable estimate of the MOC, which cannot be significantly increased using a slightly higher number of profiles. For both 26N and 36N, the standard configuration and an array relying on the full model density information provide nearly the same quality for the resulting reconstruction. However, the quality of the reconstruction at 53N is considerably less, with any numbers of profiles. To investigate this and the limited ability of the array to capture the deep return flow for the three considered latitudes, the force balance governing the MOC are analyzed.

d. Limits of the method

To identify the dominating terms governing the MOC at the different latitudes, we investigate which part of the velocity field is not captured by the array. A comparison of the estimated meridional velocities and the original meridional (model) velocities shows that errors in the mean velocity field are mainly caused by differences between the two depth-averaged fields rather than differences in the thermal wind shear or Ekman reconstruction.

A contribution by the depth-averaged velocity component to the MOC arises when (strong) currents hit sloping boundaries; i.e., in the presence of nonuniform topography and the external mode projects onto the meridional overturning (Lee and Marotzke, 1998). Its overturning contribution vanishes for zonally uniform topography. However, the link of the external mode to density differences is not as straightforward as it is difficult to separate thermal wind and ageostrophic shear contributions in section integrations (Robbins and Toole, 1997; Lee and Marotzke, 1998). Note that the spatially uniform correction applied to ensure mass balance also generates a depth-independent component in the reconstructed velocities.

In order to analyze the ability of the array to capture the external mode, the overturning contribution by the external mode is calculated for both the original model velocities and the reconstructed velocities.

$$\Psi_{ext}(y, z) = \int_{-D(x,y)}^{z} \int_{0}^{L(y,z)} \tilde{v}(x, y, z)dxdz, \tag{8}$$

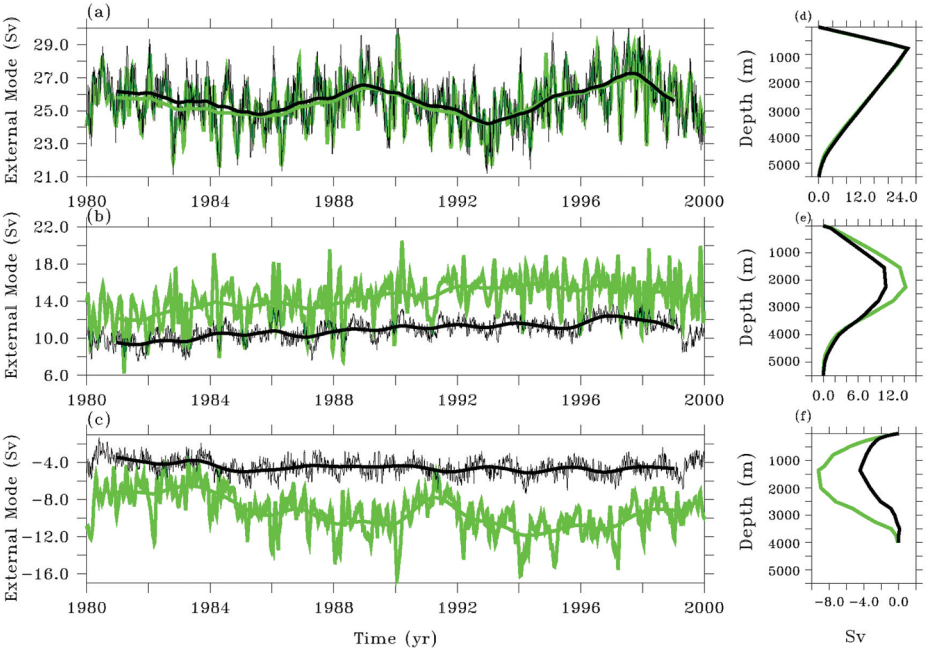

Figure 9. External mode (model, green) and estimated external mode (black). Time series of maximum is shown in (a)–(c), and the time mean vertical profile in (d)–(f); 26N: (a) and (d), 36N (b) and (e), 53N (c) and (f). Solid line in the time series of the maximum indicates two-year running mean.

where $\tilde{v}(x, y, z)$ is the depth-averaged velocity $\bar{v}(x, y) = [1/D(x, y)] \int_{-D(x,y)}^{0} v(x, y, z)dz$, evenly distributed over the water column.

Figure 9 shows a timeseries of the maximum and a time-mean vertical profile for each latitude. For 26N the external mode is reconstructed by the array, since the complete velocity pattern in the Florida Strait (where the strongest depth-averaged velocities occur) is included in the array. This is true for both the timeseries of the maximum and the vertical structure. The external mode has its maximum projection onto the MOC (of about 25 Sv) at 800 m, which coincides with the maximum depth of the Florida Strait. For 36N a small (and apart from high frequency fluctuations temporally nearly constant) part of the external mode is not estimated by the array. The vertical structure is reproduced, apart from the underestimate of the maximum of about 3 Sv. At 53N a considerable (and variable) part of the external mode is underestimated in its absolute value. In the time-mean vertical structure, the maximum value is missed by about 4 to 5 Sv.

Theoretically, the discrepancy between the original and reconstructed external mode can be added to the reconstructed overturning:

$$\Psi(y, z) = \Psi_{tw}(y, z) + \Psi_{ek}(y, z) + (\Psi_{ext_{model}}(y, z) - \Psi_{ext_{reconstr}}(y, z)), \qquad (9)$$

where $\Psi_{ext_{model}}(y, z)$ is calculated based on the meridional velocity field from the model and $\Psi_{ext_{reconstr}}(y, z)$ computed using the corrected thermal wind velocity field $v_{g_{corr}}(x, y, z)$ (Eq. 4) substituted into Eq. (8). Little effect is seen for 26N, whereas for 36N and 53N the mean value of the maximum overturning is estimated correctly when the missing depth-averaged part is taken into account (Figure not shown). Furthermore, for each of the three latitudes the deep branch of the vertical profile can be largely estimated. Thus, the overturning contribution originating from the difference between the original model and the estimated external mode does account for most of the bias in the reconstruction.

The depth-averaged velocity ($\bar{v}(x, y)$) field can presently not be measured. Under idealized circumstances, it is a sum of the velocities generated by the thermal wind and the surface wind stress plus the velocities at the bottom of the water column $v_b(x, y, z)$: $\bar{v}(x, y) = v_g(x, y, z) + v_{ek}(x, y, z) + v_b(x, y, z)$.

In this study so far, bottom velocities are assumed to be zero everywhere. The bottom of the basin was chosen as the reference level for the thermal wind calculations, i.e. integration starts at the bottom, where the geostrophic velocity is assumed to be zero. This assumption is clearly insufficient when high velocities occur at the bottom, e.g. when a deep boundary current hits a continental slope, where velocities can be as high as 10 cm s^{-1} (Lee *et al.,* 1990, 1996). Analyzing both the bottom velocity field and the depth-averaged velocity field in FLAME shows that the strongest bottom and depth-averaged velocities occur for all three latitudes at the western boundary, where currents are strongest. The time-mean bottom velocities have absolute values of up to 3 cm s^{-1} for the subtropical latitudes, and values in the range of 5 to 20 cm s^{-1} for 53N. The depth-averaged velocities exceed the bottom velocities by several tens of cm s^{-1} at the western boundary at 26N and 36N. At 53N, where the stratification is weakest, the bottom and depth-averaged velocities tend to be of the same order of magnitude at the western boundary. Away from the western boundary, the depth-averaged velocities are weaker than the bottom velocities for all three latitudes.

Instead of assuming a level of no motion at the bottom of the basin, bottom velocities could be taken as the reference level for the calculation of the thermal wind velocities estimated by the standard array. Thus, the reconstruction is now tested assuming the bottom velocities to be known (at all bottom grid points):

$$\Psi(y, z) = \Psi_{tw}(y, z) + \Psi_{ek}(y, z) + \Psi_b(y, z), \tag{10}$$

where $\Psi_b(y, z)$ is the overturning contribution originated by the bottom velocities $v_b(x, y, z)$. Again, a correction ensuring mass balance is applied prior to the integration.

$$\Psi_b(y, z) = \int_{-D(x,y,)}^{z} \int_{0}^{L(y,z)} v_{b_{corr}}(x, y, z)dxdz, \tag{11}$$

in which $v_{b_{corr}}(x, y, z)$ is the corrected bottom velocity field:

$$v_{b_{corr}}(x, y, z) = v_b(x, y, z) - \frac{\int_{-D(x,y)}^{z} \int_{0}^{L(y,z)} v_b(x, y, z)dxdz}{A}. \quad (12)$$

Velocities at the bottom of the basin are replaced by its original model value. The overturning contribution due to the bottom velocities is corrected and integrated separately to give an estimate of its relative contribution. The same result would be achieved if the bottom velocities would be included into Eq. (4) and $\Psi_{tw}(y, z)$ re-computed accordingly.

The time-mean vertical profile of $\Psi_b(y, z)$ shows a distinctive negative extreme for all three latitudes, differing considerably in its vertical placement and relative importance (Figure not shown). The time-mean maximum for 26N is -1.2 Sv and situated at a depth of about 4700 m. 36N exhibits a comparable negative maximum at a slightly shallower depth of about 4200 m. In addition, 36N shows a positive maximum of 1.6 Sv at depths ranging from 1500 m to 3000 m, where the northward boundary current hits the western slope of the basin. The time mean vertical profile for 53N has its maximum of -5.8 Sv at a depth of about 2000 m, corresponding to the strong northward boundary current hitting the western slope at this depth.

The resulting reconstruction based on the knowledge of the complete bottom velocities added to the thermal wind and Ekman reconstruction based on the standard array is shown in Figure 10. Again, the timeseries of the maximum and the time-mean vertical profile are shown for both the original and reconstructed overturning. The reconstruction follows the original overturning in both its mean value and its complete temporal variability closely for all three latitudes. The time-mean vertical profile (including the deep return flow) is reconstructed well for the three different transects.

In an attempt to reduce the amount of required information, the reconstruction is tested based on bottom velocity measurements at the locations of the profiles only. The resulting $\Psi_b(y, z)$ is very different from the one based on the complete bottom velocity field. The changes in the resulting time mean vertical profiles range from a reduction in magnitude by a factor 0.2, a displacement of the maximum in the vertical by 500 m to a change of sign for the maximum value, depending on latitude and profile placement. A reconstruction based on enhanced knowledge of bottom velocities at the western boundary shows similar behavior.

Generally, in the presence of strong bottom velocities the MOC cannot be reliably estimated based on density and wind measurements alone. Here, the MOC could be reconstructed based on the standard arrays for the individual latitudes plus additionally known bottom velocities at every zonal grid point. Currently, this is clearly an unrealistic condition, but it points to an observational requirement for the future.

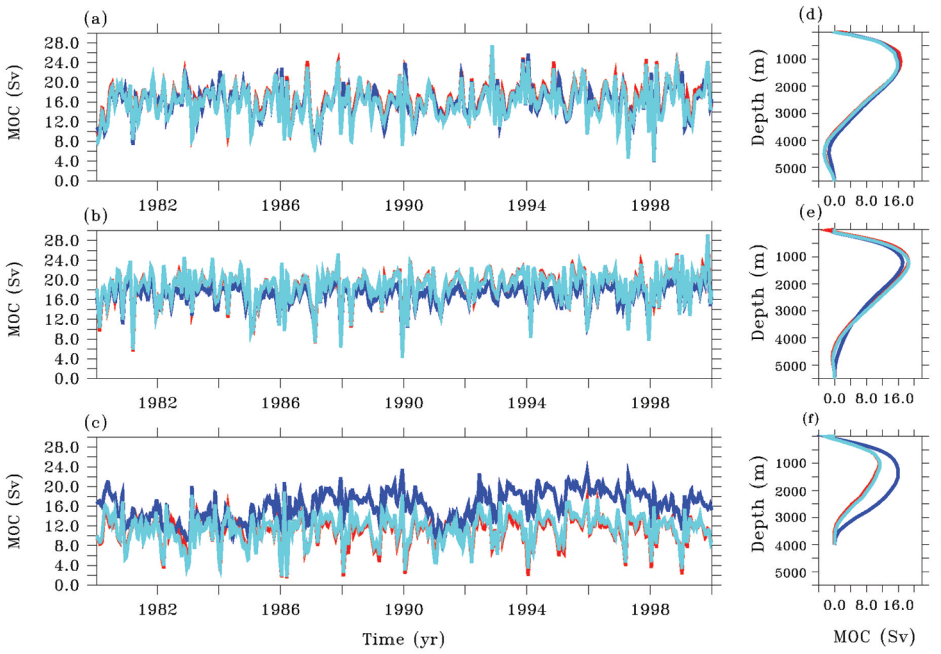

Figure 10. MOC (red), estimated transport (blue) on the basis of the standard arrays, and estimated transport on the basis of the standard arrays plus bottom velocity contribution (light blue). The estimated transport is the sum of the thermal wind and Ekman contributions. The bottom velocity contribution is based on the knowledge of the bottom velocities at every zonal grid cell. Time series of the maximum transports are shown in panels (a)–(c), and a time mean vertical profile in panels (d)–(f); 26N: (a) and (d), 36N (b) and (e), 53N: (c) and (f).

4. Meridional heat transport

The MOC is responsible for a net northward heat transport in the Atlantic of about 1 PW at 25N (Hall and Bryden, 1982), which accounts for approximately half of the total northward heat transport in the North Atlantic region, where the atmosphere provides the remaining half (Trenberth and Solomon, 1994). As variations in the ocean heat transport are expected to arise predominately from fluctuations in the velocity field (Jayne and Marotzke, 2001), the reconstructed velocity field should allow an estimate of the meridional heat transport, too. The meridional heat transport across each latitude is calculated from the reconstructed velocities and a temporally constant temperature section taken at the beginning of the "deployment period," assuming that changes in the velocity fields are rapid compared to the variations of the temperature field (Jayne and Marotzke, 2001).

Figure 11 shows the meridional heat transport based on the standard array for the three latitudes. For both 26N and 36N there is a good agreement between the estimated and modeled meridional heat transport. The mean value is reproduced well, whereas the variability is generally slightly underestimated. For 53N the reconstruction fails temporally

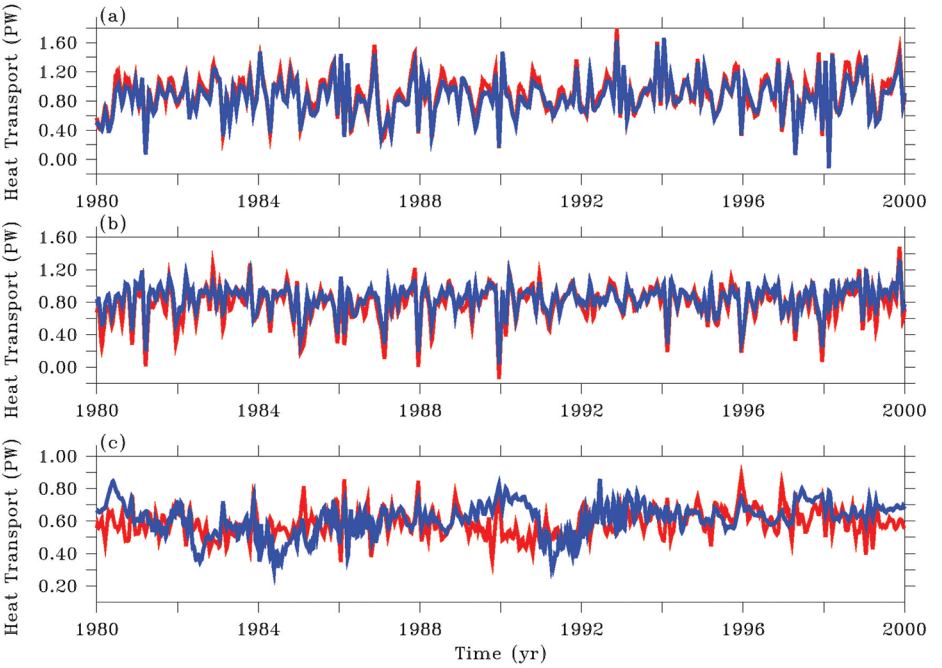

Figure 11. Meridional heat transport taken from FLAME (red) and its reconstruction (blue). The reconstruction is based on the standard array (incl Ekman velocities), combined with an initial temperature section (kept constant after first timestep). 26N: (a), 36N (b), and 53N: (c).

by up to ± 0.3 PW, these temporal over- and underestimates compensate each other resulting in a coincidentally correct reconstruction of the 20-year time-mean value of 0.6 PW.

A decomposition of the meridional heat transport into its overturning and gyre contribution (Böning and Bryan, 1996; Bryden and Imawaki, 2001) shows that the overturning contribution is reconstructed correctly in its mean value and variability for the three latitudes. The gyre component is covered for 26N (-0.1 PW) and 36N (0.05 PW) only. At 53N, in contrast, the mean value (about 0.45 PW) and the temporal variability of the gyre component are missed. The relatively large gyre component at 53N originates from strong horizontal temperature gradients, maintaining a weak stratification. The latter, in turn, allows for strong depth-independent velocities, i.e. a strong influence of the bottom topography on the velocity field, which is equivalent to a large external mode. Again, a reconstruction based on known bottom velocities captures both the mean value and the temporal variability.

5. Discussion

To assume complete knowledge of the bottom velocities is possible in a model study but not (yet) feasible in the real ocean. Bottom velocities can be obtained from direct

measurements or bottom pressure recorders (e.g. Meinen *et al.,* 2004) as they are planned to be deployed within the UK RAPID array (Natural Environment Research Council, 2003). The resolution of these measurements, however, is much coarser than the one assumed here. Generally, bottom velocities could be inferred from the seafloor pressure gradients obtained through the satellite measurements, implying geostrophy (Wahr *et al.,* 1998). Such satellite measurements with an adequate resolution of bottom pressure measurements might become available in the near future (Wahr *et al.,* 2002; Losch *et al.,* 2002). Whether those satellite-based bottom pressure measurements would be sufficient as a reference level for the thermal wind integration demands profound testing. Simulating the effect of these bottom pressure measurements is beyond the scope of this paper, since it would require disproportionate effort to derive the bottom pressure timeseries as FLAME is run with a rigid lid surface. Nevertheless, the use of bottom pressure measurements needs to be tested, possibly with a numerical model, and if applicable, the required resolution and accuracy need to be established.

Generally, an inevitable limitation to the transferability of this model-based array design study is the restricted ability of the employed model to represent the ocean circulation in its full complexity. First, despite its vigorous overturning, FLAME's representation of the deep "western" boundary current is limited, both in its respective geographical position and absolute strength: at 26N the core of the deep western boundary current is situated above the depth of the crest of the MAR, which is not in accordance with observations (e.g. Lee *et al.,* 1996). At 36N the strongest southward flow is found at the surface in the western part of the basin and a deep southward flow is found at the western slope of the MAR. Although observational evidence is limited, the results show a deep western boundary current situated beneath the northward boundary current, e.g. Roemmich and Wunsch (1985) and Rintoul and Wunsch (1991).

Second, limited spatial resolution plays a role: Although FLAME is an "eddy-permitting" model, it does not resolve eddies, and the eddy kinetic energy is still underestimated significantly (Stammer *et al.,* 1996). This should be taken into consideration for the analysis of the return flow, since the model may underestimate the variability as well as the strength of the boundary currents. Further, the spatial resolution restricts the placement of the density profiles. The total width of the western boundary current based on observations is given for 26N as about 80 km (Lee *et al.,* 1996). In contrast, FLAME's grid cell spacing at 26N is about 33 km. Hence, to cover the westernmost margin sufficiently some of the profiles are placed at adjacent grid cells. Thus, because of the model's constraints in describing the real world, some of the specific results generated by the model cannot directly be applied to the real world.

Returning to the broader perspective of observing system design, fundamentally, one wishes to determine the array configuration yielding the most comprehensive information from the observational data within the given constraints (e.g. instrumentation cost). In principle, the required objective function needs to map the dynamics of the unknown field, and the available resources adequately. To our knowledge this optimization problem has

been systematically addressed for only two idealized examples, neither directed at realistic observing system design: Barth and Wunsch (1990) used two horizontal dimensions for a time-independent experiment and Barth (1992) used a 4×4 box model. Whereas it does not seem feasible to conduct a comprehensive array design study with the the current computational resources, this might be possible in the future. However, it remains to be established if idealized, i.e. not dependent on any prior observations, optimization techniques perform better than heuristic array design based on physical intuition, taking into account our—albeit limited, but still significant—knowledge of the ocean dynamics.

Here, we test an observational method, relying on a feasible, i.e. financially realistic, experimental setup only. Whether an arbitrary latitude is suitable for potential observation requires knowledge about the real meridional velocity field (e.g. a hydrographic section). Most importantly, the magnitude of the bottom velocities and the capability of the array to capture the external mode at this latitude needs to be ensured. Further, when assessing a chosen latitude for observation, adequate placement of the profiles requires knowledge to what extent the model velocity field and the velocity field expected in the real ocean are congruent.

Simulating an array at a chosen latitude requires first the definition of a set of available resources (including potential preexisting continuous observations). Second, the profiles should be placed according to the two criteria described in the beginning of Section 3: (i) the profiles need to be placed especially in areas of high meridional velocities, and (ii) maximum spatial coverage of the basin should be ensured by the resulting array. Third, the MOC reconstruction can be computed according to Eq. (7).

Comparing the three investigated latitudes for potential observation in the real ocean suggests that 26N is superior to 36N and 53N. At 26N the MOC in FLAME can be reconstructed based on the thermal wind contribution, the Ekman contribution and continuous "measurements" of the Florida Strait transport. The bottom velocities are small and the sidewalls are steep, and the depth-averaged velocities therefore account (outside the Florida Strait) for a negligible overturning contribution only. A variety of practical reasons further supports the recommendation of 26N. First, this latitude has been occupied four times with hydrographic transects (see Section 3a). Second, the geographically confined western boundary current has been monitored by cable measurements for more than 20 years (Larsen, 1985; Baringer and Larsen, 2001). Third, 26N is close to the heat transport maximum in the Atlantic and in turn the heat transport is dominated by the MOC, i.e. the gyre component is small (Hall and Bryden, 1982).

Ultimately, one would want to extend the analysis of the force balances governing the MOC to all latitudes of the North Atlantic. In a detailed analysis of the force balances in a hierarchy of ocean models Hirschi and Marotzke (2004) suggest that this method has the potential to provide valuable information about the full meridional overturning cell. However, their analysis is not directed at observing system design and therefore does not assess which latitude would be most suitable for observation. In principle, the ratio of the overturning contribution of the external mode to the MOC could provide some measure for

this. However, the required calculation would be extremely demanding for FLAME and is left for future study.

6. Conclusions

Based on our analysis of FLAME, we conclude:

1. A small number of profiles (about 10) is sufficient to capture the main characteristics of the MOC for a single latitude in the North Atlantic as long as bottom velocities are small, here, at 26N and 36N.
2. In case of high bottom velocities the depth-averaged velocity field is not captured by the array. Thus, the MOC cannot be reliably estimated based on an array "measuring" density and surface wind stress only, here, at 53N.
3. An array that additionally incorporates the complete bottom velocity field, reproduces the MOC in its temporal and vertical structure.
4. Effectively, we confirm that the thermal wind and the Ekman contributions are the dominant terms in the force balance governing the MOC, with sometimes significant but generally smaller contributions from other terms.
5. Of the three latitudes analyzed here, 26N is the one most suitable for observation in the real ocean: it allows comparison with historical data, the western boundary current has been monitored continuously, and the depth-averaged velocity field is—in FLAME—largely captured by the array.

Acknowledgments. We wish to thank Harry Bryden for stimulating discussions and Johann Jungclaus for helpful comments on the manuscript. We are indebted to the two reviewers for their thorough reviews. This work was supported by the Natural Environment Research Council (NERC), the University of Southampton and the Max Planck Society.

REFERENCES

Alley, R. B., J. Marotzke, W. D. Nordhaus, J. T. Overpeck, D. M. Peteet, R. A. Pielke Jr., R. T. Pierrehumbert, P. B. Rhines, T. F. Stocker, L. D. Talley and J. M. Wallace. 2003. Abrupt climate change. Science, *299,* 2005–2010.

Baringer, M. O. and J. C. Larsen. 2001. Sixteen years of Florida Current transport at 27°N. Geophys. Res. Lett., *28,* 3179–3182.

Barnier, B., L. Siefriedt and P. Marchesiello. 1995. Thermal forcing for a global ocean circulation model using a three-year climatology of ECMWF analyses. J. Mar. Syst., *6,* 363–380.

Barth, N. H. 1992. Oceanographic experiment design II: Genetic algorithms. J. Atmos. Oceanic Tech., *9,* 434–443.

Barth, N. and C. Wunsch. 1990. Oceanographic experiment design by simulated annealing. J. Phys. Oceanogr., *20,* 1249–1263.

Beckmann, A. and R. Döscher. 1997. A method for improved representation of dense water spreading over topography in geopotential-coordinate models. J. Phys. Oceanogr., *27,* 581–591.

Beismann, J. and R. Redler. 2003. Model simulations of CFC uptake in North Atlantic deep water:

Effects of parametrizations and grid resolution. J. Geophys. Res., *108* (C5), 3159, doi: 10.1029/2001JC001253.

Bennett, A. F. 1985. Array design by inverse methods. Progr. Oceanogr., *15,* 129–156.

Bennett, A. F. and P. C. McIntosh. 1982. Open ocean modelling as an inverse problem: Tidal theory. J. Phys. Oceanogr., *12,* 1004–1018.

Böning, C. W., C. Dieterich, B. Barnier and Y. Jia. 2001. Seasonal cycle of meridional heat transport in the subtropical North Atlantic: A model intercomparison in relation to observations near 25N. Progr. Oceanogr., *48,* 231–253.

Böning, C. W. and F. O. Bryan. 1996. Large-scale transport processes in high-resolution circulation models, *in* The Warmwatersphere of the North Atlantic Ocean, W. Krauss, ed., Gebrüder Bornträger, 91–128.

Boyer, T. P. and S. Levitus. 1997. Objective analyses of temperature and salinity for the world ocean on a 1/4 degree grid, NOAA Atlas NESDIS 11. U.S. Dep. of Comm., 55 pp.

Bretherton, F. P., R. E. Davis and C. B. Fandry. 1976. A technique for objective analysis and design of oceanographic experiments applied to MODE-73. Deep-Sea Res., *23,* 559–582.

Bryden, H. L. and S. Imawaki. 2001. Ocean heat transport, *in* Ocean Circulation and Climate: Observing and Modelling the Global Ocean, G. Siedler, J. Church, and J. Gould, eds., Academic Press, 455–474.

Chereskin, T. K., W. D. Wilson, H. L. Bryden, A. Field and J. Morrison. 1997. Observations of the Ekman balance at 8°30′N in the Arabian Sea during the 1995 southwest monsoon. Geophys. Res. Lett., *21,* 2541–2544.

Cox, M. D. 1987. Isopycnal diffusion in a *z*-coordinate model. Ocean Model., *74,* 1–5.

Dansgaard, W., S. J. Johnsen, H. B. Clausen, D. Dahl-Jensen, N. S. Gundestrup, C. U. Hammer, C. S. Hvidberg, J. P. Steffensen, A. E. Sveinbjoernsdottir, J. Jouzel and G. Bond. 1993. Evidence for general instability of past climate from a 250-kyr ice-core record. Nature, *364,* 218–220.

Dengg, J., C. Böning, U. Ernst, R. Redler and A. Beckmann. 1999. Effects of an improved model representation of overflow water on the Subpolar North Atlantic. Inter. WOCE Newsletter, *37,* 10–15.

Deutsch, C., M. G. Hall, D. F. Bradford and K. Keller. 2002. Detecting a potential collapse of the North Atlantic thermohaline circulation: Implications for the design of an ocean observing system. Paper presented at the EMF Summer Workshop "Climate Change Impacts and Integrated Assessment VIII" Snowmass, Colorado, available at: http://www.geosc.psu.edu/~kkeller.

Dobrolyubov, S. A., S. S. Lappo, E. G. Morozov, A. V. Sokov, V. P. Tereschenkov and S. M. Shapovalov. 2002. Water structure in the North Atlantic in 2001 based on a transatlantic section along 53°N. Oceanology, *382,* 543–546.

Eden, C. and J. Willebrand. 2001. Mechanism of interannual to decadal variability of the North Atlantic circulation. J. Climate, *14,* 2266–2280.

Fischer, J., F. A. Schott and M. Dengler. 2004. Boundary circulation at the exit of the Labrador Sea. J. Phys. Oceanogr., (in press).

Ganachaud, A. and C. Wunsch. 2000. Improved estimates of global ocean circulation, heat transport and mixing from hydrographic data. Nature, *408,* 453–457.

——2002. Oceanic nutrient and oxygen transports and bounds on export production during the World Ocean Circulation Experiment. Global Biogeochem. Cycles, *16,* 1057–1071.

Guinehut, S., G. Larnicol and P. Y. Le Traon. 2002. Design of an array of profiling floats in the North Atlantic from model simulations. J. Mar. Syst., *35,* 1–9.

Hackert, E. C., R. N. Miller and A. J. Busalacchi. 1998. An optimized design for a moored array in the tropical Atlantic Ocean. J. Geophys. Res., *103* (C4), 7491–7509.

Hall, M. M. and H. L. Bryden. 1982. Direct estimates and mechanisms of ocean heat transport. Deep-Sea Res., *29* (3A), 339–359.

Harrison, D. E. 1989. Local and remote forcing of ENSO ocean waveguide response. J. Phys. Oceanogr., *19,* 691–695.

Harrison, D. E., W. S. Kessler and B. J. Giese. 1989. Ocean circulation and model hindcasts of the 1982–83 El Nino: Thermal variability along the ship-of-opportunity tracks. J. Phys. Oceanogr., *19,* 397–418.

Heinrich, H. 1988. Origin and consequences of cyclic ice rafting in the northeast Atlantic Ocean during the past 130,000 years. Quatern. Res., *29,* 142–152.

Hirschi, J., J. Baehr, J. Marotzke, J. Stark, S. Cunningham and J.-O. Beismann. 2003. A monitoring design for the Atlantic meridional overturning circulation. Geophys. Res. Lett., *30* (7), 1413, doi: 10.1029/2002GL016776.

Hirschi, J. and J. Marotzke. 2004. Strength and variability of the meridional overturning circulation inferred from thermal wind and Ekman transports. (in preparation).

Jayne, S. R. and J. Marotzke. 2001. The dynamics of ocean heat transport variability. Rev. Geophys., *39,* 385–411.

Kalnay, E., M. Kanamitsu, R. Kistler, W. Collins, D. Deaven, L. Gandin, M. Iredell, S. Saha, G. White, J. Woollen, Y. Zhu, M. Chelliah, W. Ebisuzaki, W. Higgins, J. Janowiak, K. C. Mo, C. Ropelewski, J. Wang, A. Leetmaa, R. Reynolds, R. Jenne and D. Joseph. 1996. The NCEP 40-year reanalysis project. Bull. Amer. Meteor. Soc., *77,* 437–471.

Köhl, A. and D. Stammer. 2004. Optimal observations for variational data assimilation. J. Phys. Oceanogr., *34,* 529–542.

Koltermann, K. P., A. V. Tereschenkov, S. A. Dobroliubov, K. Lorbacher, and A. Sy. 1999. Decadal changes in the thermohaline circulation of the North Atlantic. Deep-Sea Res., II, *46,* 109–138.

Larsen, J. C. 1985. Florida current volume transports from voltage measurements. Science, *277,* 302–304.

Lavin, A., H. L. Bryden and G. Parilla. 1998. Meridional transport and heat flux variations in the subtropical North Atlantic. The Global Atmos. Ocean Syst., *6,* 231–241.

Lee, T. and J. Marotzke. 1998. Seasonal cycles of meridional overturning and heat transport of the Indian Ocean. J. Phys. Oceanogr., *28,* 923–943.

Lee, T. N., W. Johns, F. Schott and R. Zantopp. 1990. Western boundary current structure and variability east of Abaco, Bahamas at 26°N. J. Phys. Oceanogr., *20,* 446–466.

Lee, T. N., W. E. Johns, R. J. Zantopp and E. R. Fillenbaum. 1996. Moored observations of western boundary current variability and thermohaline circulation at 26.5°N in the subtropical North Atlantic. J. Phys. Oceanogr., *26,* 962–983.

Levitus, S., T. Boyer and R. Burgett. 1994. World ocean atlas 1994, Vol. 3: Salinity, NOAA Atlas NESDIS 3. U.S. Dept. of Comm., 99 pp.

Losch, M., R. Redler and J. Schröter. 2002. Estimating a mean ocean state from hydrography and sea-surface height with a nonlinear inverse model: Twin experiments with a synthetic dataset. J. Phys. Oceanogr., *32,* 2096–2112.

MacDonald, A. M. 1998. The global ocean circulation: A hydrographic estimate and regional analysis. Progr. Oceanogr., *41,* 281–382.

MacDonald, A. M. and C. Wunsch. 1996. An estimate of global ocean circulation and heat fluxes. Nature, *382,* 436–439.

Marotzke, J. 1997. Boundary mixing and the dynamics of three-dimensional thermohaline circulations. J. Phys. Oceanogr., *27,* 1713–1728.

——2000. Abrupt climate change and thermohaline circulation: Mechanisms and predictability. Proc. Nat. Acad. Sci., *97,* 1347–1350.

Marotzke, J., S. A. Cunningham and H. L. Bryden. 2002. Monitoring the Atlantic meridional overturning circulation at 26.5°N. Proposal accepted by the Natural Environment Research Council (UK), available at: http://www.nerc.ac.uk/funding/thematics/rcc/Scienceplan.shtml.

Marotzke, J., R. Giering, K. Q. Zhang, D. Stammer, C. Hill and T. Lee. 1999. Construction of the adjoint MIT ocean general circulation model and application to Atlantic heat transport sensitivity. J. Geophys. Res., *104,* 29,529–29,547.

Marotzke, J. and B. A. Klinger. 2000. The dynamics of equatorially asymmetric thermohaline circulations. J. Phys. Oceanogr., *30,* 955–970.

McCreary, J. P. and P. Lu. 1994. Interaction between the Subtropical and Equatorial ocean circulations: The Subtropical Cell. J. Phys. Oceanogr., *24,* 466–497.

McIntosh, P. C. 1987. Systematic design of observational arrays. J. Phys. Oceanogr., *17,* 885–902.

McTaggert, K. E., G. C. Johnson, C. I. Fleurant and M. O. Baringer. 1999. CTD/O_2 measurements collected on a climate and global change cruise along 24°N in the Atlantic Ocean (WOCE section A6) during January–February 1998, Contribution No. 2056. NOAA/Pacific Marine Environmental Laboratory, 30 pp.

Meinen, C. S., S. L. Garzoli, W. E. Johns and M. O. Baringer. 2004. Transport variability of the Deep Western Boundary Current and the Antilles Current off Abaco Island, Bahamas. Deep-Sea Res. I, (submitted).

National Research Council (NRC). 2002. Abrupt Climate Change: Inevitable Surprises. National Academy Press, 230 pp.

Natural Environment Research Council. 2003. Natural Environment Research Council (NERC), UK, thematic programme: Rapid Climate Change, available at: http://www.nerc.ac.uk/funding/thematics/rcc/Scienceplan.shtml.

Pacanowski, R. 1995. MOM2 documentation (User's guide and reference manual), GFDL Ocean Technical Reports 3. Princeton University.

Poje, A. C., M. Toner, A. D. Kirwan Jr. and C. K. R. T. Jones. 2002. Drifter launch strategies based on Lagrangian templates. J. Phys. Oceanogr., *32,* 1855–1869.

Redi, M. H. 1982. Oceanic isopycnal mixing by coordinate rotation. J. Phys. Oceanogr., *12,* 1154–1158.

Rintoul, S. R. and C. Wunsch. 1991. Mass, heat, oxygen and nutrient fluxes and budgets in the North Atlantic Ocean. Deep-Sea Res., *38* (Suppl. 1), S355–S377.

Robbins, P. E. and J. M. Toole. 1997. The dissolved silica budget as a constraint on the meridional overturning circulation of the Indian Ocean. Deep-Sea Research I, *44* (5), 879–906.

Roemmich, D. and C. Wunsch. 1985. Two transatlantic sections: Meridional circulation and heat flux in the subtropical North Atlantic Ocean. Deep-Sea Research, *32* (6), 619–664.

Sato, O. T. and T. Rossby. 2000. Seasonal and low-frequency variability of the meridional heat flux at 36°N in the North Atlantic. J. Phys. Oceanogr., *30,* 606–621.

Scheinert, M. 2003. Mechanismen niederfrequenter Schwankungen des westlichen Randstroms im subpolaren Nordatlantik, Dipl. thesis. IfM Kiel, 51 pp.

Schröter, J. and C. Wunsch. 1986. Solution of non-linear finite difference ocean models by optimization methods with sensitivity and observational strategy analysis. J. Phys. Oceanogr., *16,* 1855–1874.

Stammer, D., R. Tokmakian, A. Semtner and C. Wunsch. 1996. How well does a 1/4° global circulation model simulate large-scale oceanic observations? J. Geophys. Res., *101,* 25779–25811.

Talley, L. 2003. Shallow, intermediate, and deep overturning components of the global heat budget. J. Phys. Oceanogr., *33,* 530–560.

Trenberth, K. E. and A. Solomon. 1994. The global heat balance: Heat transport in the atmosphere and ocean. Climate Dyn., *10,* 107–134.

Wahr, J. M., S. R. Jayne and F. O. Bryan. 2002. A method of inferring changes in deep ocean currents from satellite measurements of time-variable gravity. J. Geophys. Res., *107* (C12), 3218, doi: 1029/2001JC001274.

Wahr, J., M. Molenaar and F. Bryan. 1998. Time variability of the Earth's gravity field: Hydrological and oceanic effects and their possible detection using GRACE. J. Geophys. Res., *103* (B3), 30,205–30,229.

Willebrand, J., B. Barnier, C. Böning, C. Dietrich, P. D. Killworth, C. le Provost, Y. Jia, J.-M. Molines and A. L. New. 2001. Circulation characteristics in three eddy-permitting models of the North Atlantic. Progr. Oceanogr., *48,* 123–161.

Wood, R. A., A. B. Keen, J. F. B. Mitchell and J. M. Gregory. 1999. Changing spatial structure of the thermohaline circulation in response to atmospheric CO_2 forcing in a climate model. Nature, *399,* 572–575.

Received: *7 January, 2004;* revised: *22 March, 2004.*